

## Transient growth in Taylor-Couette flow of a Bingham fluid

 Cheng Chen,<sup>1,\*</sup> Zhen-Hua Wan,<sup>2</sup> and Wei-Guo Zhang<sup>1</sup>
<sup>1</sup>*Low Speed Aerodynamics Institute, China Aerodynamics Research and Development Center, Mianyang, Sichuan 622762, China*
<sup>2</sup>*Department of Modern Mechanics, University of Science and Technology of China, Hefei, Anhui 230027, China*

(Received 1 March 2014; published 13 April 2015)

In this paper we investigate linear transient growth of perturbation energy in Taylor-Couette flow of a Bingham fluid. The effects of yield stress on transient growth and the structure of the optimal perturbation are mainly considered for both the wide-gap case and the narrow-gap case. For this purpose we complement the linear stability of this flow subjected to axisymmetric disturbances, presented by Landry *et al.* [M. P. Landry, I. A. Frigaard, and D. M. Martinez, *J. Fluid Mech.* **560**, 321 (2006)], with the transient growth characteristics of both axisymmetric and nonaxisymmetric perturbations. We obtain the variations of the relative amplitude of optimal perturbation with yield stress, analyze the roles played by the Coriolis force and the additional stress in the evolution of meridional perturbations for the axisymmetric modes, and give the explanations for the possible change of the optimal azimuthal mode (featured by the maximum optimal energy growth  $G_{\text{opt}}$ ) with yield stress. These results might help us in the understanding of the effect of fluid rheology on transient growth mechanism in vortex flows.

 DOI: [10.1103/PhysRevE.91.043202](https://doi.org/10.1103/PhysRevE.91.043202)

PACS number(s): 47.20.Qr

### I. INTRODUCTION

A comprehensive understanding of turbulent phenomena in Taylor-Couette flow has received considerable recent attention [1–6] since the sudden transition to spiral turbulence in the linearly stable region was reported by Coles [7] and Van Atta [8] in the 1960s and later on by Andereck and co-workers [9,10] in the 1980s. This subcritical transition cannot be explained by classical eigenvalue analysis, whereas it may be associated with substantial transient growth that even very small perturbations may suffer due to the non-normality of the linearized operator [11]. Hristova *et al.* [12,13] and Meseguer [14,15] have investigated transient growth in Taylor-Couette flow for counterrotation scenarios and demonstrated that the lift-up mechanism is responsible for the short-term growth of initial axisymmetric perturbations and the formation of azimuthal streaks.

Investigation of the non-Newtonian Bingham case from this point of view is lacking. Landry *et al.* [16,17] performed a linear stability analysis of Taylor-Couette flow of a Bingham fluid subjected to axisymmetric disturbances. The most interesting feature of the results is the nonmonotonicity of the critical inner cylinder Reynolds number for wide-gap corotating cylinders as the yield stress is increased, much like that observed in the context of spiral Couette flow [18]. It is the only situation that we know of where a yield stress fluid flow is less stable than the corresponding Newtonian fluid flow, in contrast to the conclusion by Graebel [19]. With this in mind, it is naturally desirable to study the effects of yield stress on the transient growth characteristics in the corotating cylinder regime as well as the counterrotating cylinder regime, with the aim to gain further insight into the stability of Taylor-Couette flow of a Bingham fluid. In this paper we present some general theoretical results to depict the influence of the Bingham number  $B$  on the transient growth and on the optimal perturbation, i.e., the initial conditions that provide the maximal energy growth, which is proved to be affected by the Bingham number evidently in the case of plane Bingham-Poiseuille flow [20].

### II. PROBLEM FORMULATION

We consider the flow of an incompressible Bingham fluid with a yield stress  $\tau_y$ , plastic viscosity  $\mu_p$ , and density  $\rho$  between two concentric rotating cylinders whose angular velocities are  $\Omega_1$  and  $\Omega_2$ , respectively. Following the analytical formulation by Chossat and Iooss [21] and using  $d = R_2^* - R_1^*$ ,  $\Omega_1 R_1^*$ , and  $\mu_p \Omega_1 R_1^* / d$  as characteristic scales for space, velocity, and the deviatoric stress, the constitutive equations can be written as

$$\begin{aligned} \tau_{ij} &= \mu \dot{\gamma}_{ij} = \left(1 + \frac{B}{\dot{\gamma}}\right) \dot{\gamma}_{ij} \quad \text{for } \tau > B, \\ \dot{\gamma} &= 0 \quad \text{for } \tau \leq B, \end{aligned}$$

where  $\dot{\gamma}$  and  $\tau$  are the second invariants of the rate of strain and deviatoric stress tensors and  $\mu$  is the effective viscosity. The Bingham number  $B$  above represents a ratio of yield stress to viscous stress, defined as

$$B = \frac{\tau_y d}{\mu_p R_1^* \Omega_1}.$$

Defining the outer boundary of the yielded region as

$$R_o = \min \left\{ \frac{\eta}{1-\eta} \sqrt{\frac{|\tau_i|}{B}}, \frac{1}{1-\eta} \right\},$$

the basic velocity profile  $\mathbf{U} = (U, V, W)$  in directions  $(r, \theta, z)$  is found to be [17,22]

$$\begin{aligned} U &= 0, \\ V(r) &= \frac{\text{Re}_2(1-\eta)}{\text{Re}_1} r + \frac{\tau_i \eta^2 r}{2(1-\eta)^2} \left( \frac{1}{R_o^2} - \frac{1}{r^2} \right) \\ &\quad + Br \ln \left( \frac{R_o}{r} \right) \text{sgn}(\tau_i), \quad R_1 \leq r \leq R_o, \\ W &= 0, \end{aligned} \tag{1}$$

where  $\eta = R_1^*/R_2^*$  is the radius ratio (inner cylinder radius to outer cylinder radius),  $R_1 = \eta/(1-\eta)$  is the dimensionless inner radius, and  $\tau_i$  is the inner wall shear stress. The parameters  $\text{Re}_1 = \rho R_1^* \Omega_1 d / \mu_p$  and  $\text{Re}_2 = \rho R_2^* \Omega_2 d / \mu_p$  are the

\*Corresponding author: chief@mail.ustc.edu.cn

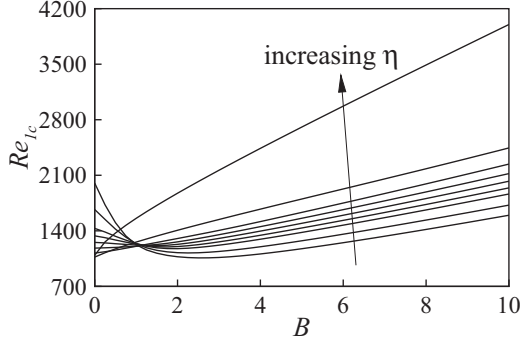


FIG. 1. Marginal stability curves in the  $(B, \text{Re}_1)$  plane for  $\eta = 0.5, 0.6, 0.7, 0.75, 0.8, 0.85, 0.9, 0.95,$  and  $0.99$  with  $\text{Re}_2 = 1000$ .

inner and outer cylinder Reynolds numbers, respectively. Two radius ratios 0.5 and 0.99 are mainly considered in this study, corresponding to the work by Hristova *et al.* [12]. Also, these two values usually represent the wide-gap case and the narrow-gap case in the Taylor-Couette problem [23] and there exists a smooth transition of the behavior of the Bingham fluid between the cases presented here according to our computations. As shown in Fig. 1, the nonmonotonicity of the critical Reynolds number  $\text{Re}_{1c}$  for linear axisymmetric disturbances at fixed  $\text{Re}_2$  ( $\text{Re}_2 = 1000$ ), i.e., the destabilizing effect of increasing  $B$ , disappears gradually with increasing  $\eta$ . Likewise, gradual variation (with  $\eta$ ) of the transient growth behavior is revealed by nonmodal analysis, which also shows that the situation with a smaller radius ratio ( $\eta = 0.4$ ) is nearly the same as for the wide-gap case (the relevant results are not given here).

For our analysis, the mean flow is supposed to be perturbed by a small disturbance of velocity  $(u, v, w)e^{i(m\theta + kz)}$  and pressure  $pe^{i(m\theta + kz)}$ , where  $m$  and  $k$  are the azimuthal and axial wave numbers, respectively. The evolution equations in terms of the complex amplitudes  $\mathbf{u} = (u, v, w)$  are written

$$\frac{\partial u}{\partial t} = -Dp - \text{Re}_1 \Omega (imu - 2v) + \left( DD_* - k^2 - \frac{m^2}{r^2} \right) u - \frac{2imv}{r^2} + B\phi_r, \quad (2)$$

$$\frac{\partial v}{\partial t} = -\frac{imp}{r} - \text{Re}_1 (uD_*V + imv\Omega) + \left( DD_* - k^2 - \frac{m^2}{r^2} \right) v + \frac{2imu}{r^2} + B\phi_\theta, \quad (3)$$

$$\frac{\partial w}{\partial t} = -ikp - \text{Re}_1 imw\Omega + \left( D_*D - k^2 - \frac{m^2}{r^2} \right) w + B\phi_z, \quad (4)$$

with  $\dot{\gamma} = \dot{\gamma}(\mathbf{U})$ , where

$$\phi_r = \frac{1}{r} D \left( \frac{2rDu}{\dot{\gamma}} \right) + \frac{1}{\dot{\gamma}} \left( ikDw - k^2u - \frac{2(imv + u)}{r^2} \right), \quad (5)$$

$$\phi_\theta = \frac{1}{\dot{\gamma}} \left( \frac{2(imu - m^2v)}{r^2} - \frac{kmw}{r} - k^2v \right), \quad (6)$$

$$\phi_z = \frac{1}{r} D \left( \frac{r(iku + Dw)}{\dot{\gamma}} \right) - \frac{1}{\dot{\gamma}} \left( \frac{m^2w}{r^2} + \frac{kmv}{r} + 2k^2w \right), \quad (7)$$

where  $\Omega = V/r$  is the angular speed,  $D = d(\cdot)/dr$ , and  $D_* = d(\cdot)/dr + (\cdot)/r$ . Spatial discretization is achieved here through a standard Chebyshev spectral collocation method [24]. Note that for the case that the basic flow has a partial plug in the annulus  $r \in [R_o, 1/(1 - \eta)]$ , besides the boundary condition  $\mathbf{u}(R_1) = \mathbf{u}(R_o) = 0$ , additional conditions also arise from continuity of stress at the perturbed yield surface [16, 17].

To measure the growth of an arbitrary initial disturbance, we use the energy norm

$$E(\mathbf{u}) = \|\mathbf{u}\|_E^2 = \frac{1}{2} \int_{R_1}^{R_o} (|u|^2 + |v|^2 + |w|^2) r dr. \quad (8)$$

The maximal energy growth  $G(t)$  for  $\mathbf{u}$  evolving according to (2)-(4) is defined by maximizing the ratio between the energy norm of the perturbation at time  $t$  and its initial norm

$$G(t) = \sup_{\mathbf{u}(0) \neq 0} \frac{\|\mathbf{u}(t)\|_E^2}{\|\mathbf{u}(0)\|_E^2}, \quad (9)$$

which is calculated using the method described by Schmid and Henningson [25]. The optimal energy growth in time is defined as  $G_{\text{opt}} = G(t_{\text{opt}}) = \sup_{t \geq 0} G(t)$ , where  $t_{\text{opt}}$  is the corresponding optimal time. The optimal perturbation, denoted by  $\mathbf{u}(0)$ , is the normalized initial condition, which achieves the maximum (sup) for  $t = t_{\text{opt}}$ .

Our target is to study the effect of yield stress on transient growth in Taylor-Couette flow. Therefore, a wide range of the Bingham number is investigated, varying from 0 to 10. For corotating cylinders, the outer cylinder Reynolds number is fixed as  $\text{Re}_2 = 1000$ , for which the increase in the rate of strain of the basic flow amplifies the transfer of energy from the basic flow to the perturbation, leading to the destabilizing effect of increasing  $B$  [17]. In contrast, for counterrotating cylinders, the outer cylinder Reynolds number is set to  $\text{Re}_2 = -1000$ .

### III. RESULTS AND DISCUSSIONS

We now consider the growths obtained by solving the transient growth problem; we first focus on axisymmetric ( $m = 0$ ) optimal modes for corotating cylinders. Figure 2 plots the maximum  $G_{\text{max}}(B, \text{Re}_1) = \sup_k G_{\text{opt}}(k, B, \text{Re}_1)$  for all  $k$  as a function of  $B$  and  $\text{Re}_1$ . Inside the shaded region, the flow is linearly unstable with respect to axisymmetric perturbations. The boundary of this region gives the critical inner cylinder Reynolds number  $\text{Re}_{1c}(B)$  as a function of Bingham number  $B$ . For a wide-gap case ( $\eta = 0.5$ ), at large enough  $\text{Re}_1$ ,  $G_{\text{max}}$  increases rapidly with  $B$  and terminates by meeting the linear instability boundary, while  $G_{\text{max}}$  decreases with increasing  $B$  over the shaded region. This nonmonotonicity of  $G_{\text{max}}$  is obviously related to that of the critical Reynolds number. At relatively small  $\text{Re}_1$ , it is found that  $G_{\text{max}}$  is reduced monotonically as  $B$  is increased. For a narrow-gap case ( $\eta = 0.99$ ),  $G_{\text{max}}$  at fixed  $\text{Re}_1$  decreases quite slowly with increasing  $B$ , despite the magnitude of  $\text{Re}_1$ , as can be seen from Fig. 2(b).

The effect of the yield stress on the relative amplitude of the azimuthal and radial directions of the optimal perturbation (the modulus)  $|v|/|v|_{\text{max}}$ ,  $|u|/|v|_{\text{max}}$  is shown in Fig. 3 for the

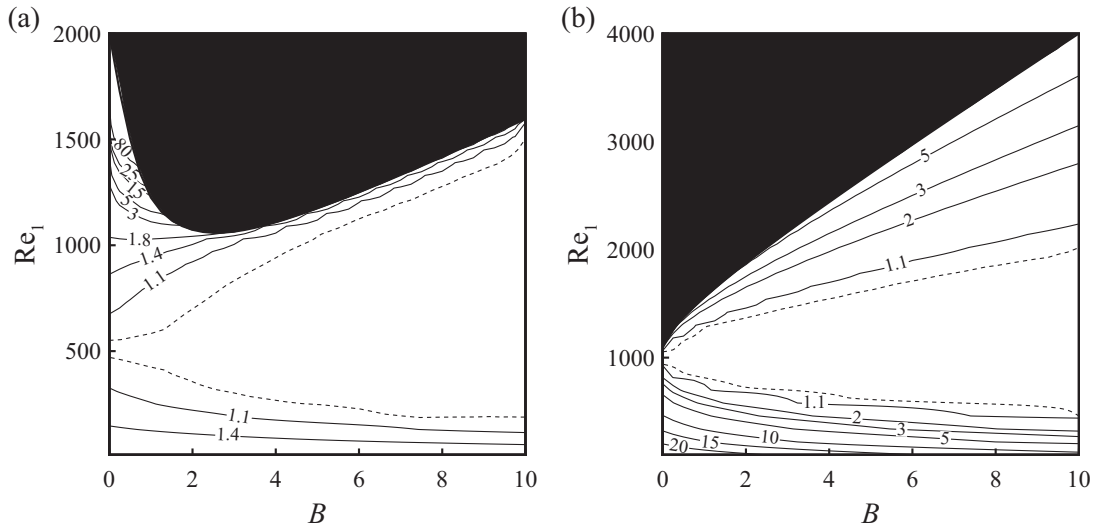


FIG. 2. Constant maximum of optimal growth  $G_{\max}$  in the  $(B, \text{Re}_1)$  plane for (a)  $\eta = 0.5$  and (b)  $\eta = 0.99$ . The dashed lines correspond to  $G_{\max}(B, \text{Re}_1) = 1$ .

wide-gap case with two different values of  $\text{Re}_1$ . The choice of  $k$ , which is proven not to affect the qualitative results in the paper, corresponds to the maximum  $G_{\max}$  at  $B = 9.5$ . For larger  $\text{Re}_1$ , the single peak of the perturbed azimuthal velocity is shifted toward the inner cylinder with increasing  $B$ , whether transient growth magnitude is increasing or decreasing; at lower  $\text{Re}_1$ , the larger peak is also shifted toward the inner cylinder by strong yield stress and the lower one is dissipated progressively. The shifting of the peak values is also evident for the amplitude of the perturbed radial velocity, as shown in Figs. 3(b) and 3(d). It is noteworthy that the increase of yield stress with larger  $\text{Re}_1$  would result in a nonmonotonic

change in the magnitude of the radial perturbation. For the narrow-gap case, both the azimuthal and radial components of the optimal perturbation are of single-peak shape (see Fig. 4) as in the Newtonian flow [14]. As shown in Fig. 4(a), the radial position of the maximum value of the perturbed azimuthal velocity is shifted toward the outer cylinder, depending upon  $B$ . Further, the amplitudes of the perturbed velocities in the meridian plane are larger than that of the azimuthal velocity within the selected range of Bingham numbers [Fig. 4(b)], whereas the opposite is true at large  $\text{Re}_1$  in the wide-gap case. This implies that the optimal perturbations occurring for the two cases may have different ways of energy evolution.

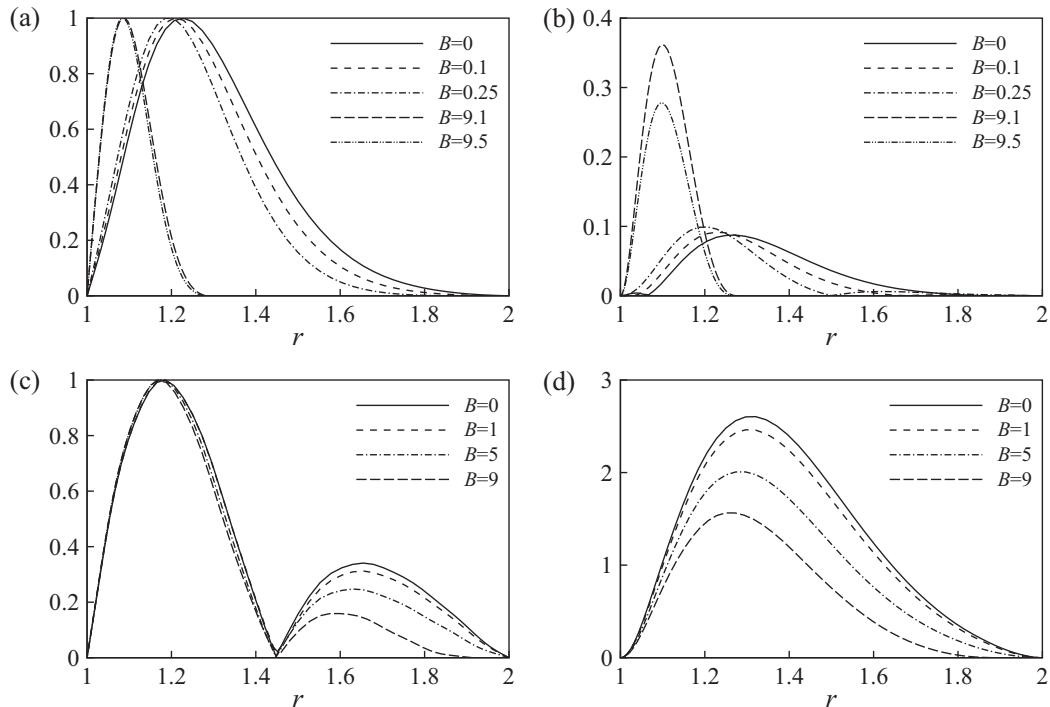


FIG. 3. Amplitudes of the (a) and (c) azimuthal and (b) and (d) radial directions of the optimal perturbation with  $\eta = 0.5$  at (a) and (b)  $\text{Re}_1 = 1510$  and  $k = 10.34$  and (c) and (d)  $\text{Re}_1 = 70$  and  $k = 5.04$ .

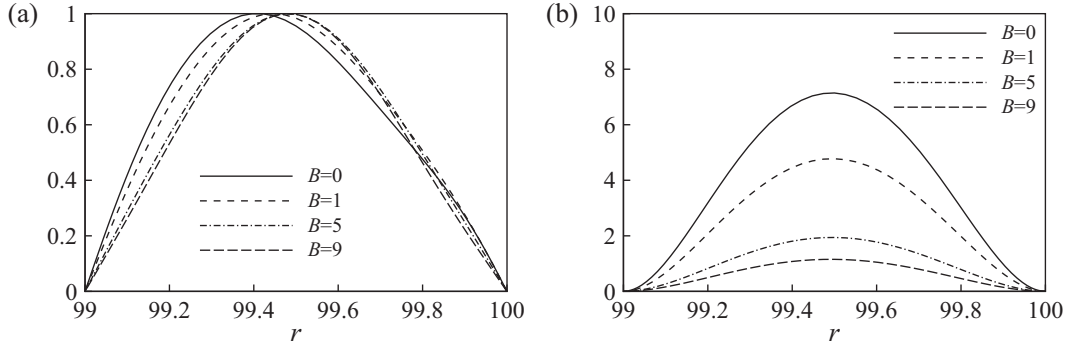


FIG. 4. Amplitudes of the (a) azimuthal and (b) radial direction of the optimal perturbation with  $\eta = 0.99$ ,  $Re_1 = 340$ , and  $k = 2.82$ .

The meridional velocity fields and contours of azimuthal velocity of the optimal input  $\mathbf{u}(0)$  are illustrated in Fig. 5 in the absence of yield stress. For the wide-gap case, the meridional velocity fields consist of three arrays of vortices, among which the first and third arrays (running left to right) occupy only a very small radial range and rotate in the direction opposite to that of the second one. In contrast, for the narrow-gap case, only one array of vortices is observed with the azimuthal component significantly weaker. Further, the azimuthal components of the optimal inputs, shown in Figs. 5(b) and 5(d), are in phase opposition with the vortices.

To understand the evolutionary behavior of the optimal perturbation, we show the time variation of the energies in the meridional components  $E_{rz} = \frac{1}{2} \int_{R_1}^{R_0} (|u|^2 + |w|^2) r dr$  and in the azimuthal component  $E_\theta = \frac{1}{2} \int_{R_1}^{R_0} |v|^2 r dr$ . For the wide-gap case, in the case of zero yield stress, the optimal perturbation  $\mathbf{u}(0)$  is concentrated primarily in the azimuthal component ( $E_\theta \gg E_{rz}$ ), as shown in Fig. 6(a). With time,  $E_\theta$  decreases rapidly and  $E_{rz}$  increases. That is, the energy of the azimuthal direction of the flow is transferred to the meridional components by the anti-lift-up mechanism found by Antkowiak and Brancher [26,27]. This phenomenon is usually linked to the generation of the vortex rings, an intrinsic feature of vortices, and is not typically reported for Taylor-Couette flow. A similar trend is found in the energy growth curves with  $B = 0.25$ , in the range of Bingham number where  $G_{max}$  increases with increasing  $B$ . Nevertheless, while strong yield stress fluid is considered ( $B = 9.1$ ), the situation is quite different. Initially, the flow field is still dominated by the azimuthal velocity ( $E_\theta \gg E_{rz}$ ). As time increases,  $E_{rz}$  decreases rapidly, going with increasing  $E_\theta$ . Subsequently, both of them decay as predicted by the linear stability analysis. These results would imply that for the wide-gap case, when yield stress is strong enough, the lift-up mechanism is responsible for transient growth instead of the anti-lift-up scenario. Figure 6(b) plots the  $E_{rz}$  and  $E_\theta$  curves corresponding to three values of  $B$  for the narrow-gap case. Obviously, yield stress, strong or weak, does not change the fact that the short-time energy growth in asymptotically stable flow regimes is due to the lift-up effect. In addition, it is clear that both  $E_{rz}$  and  $E_\theta$  are greatly reduced by strong yield stress, which brings positive dissipation to the kinetic energy growth of the perturbations [17].

Before examining the physical growth mechanism in this axisymmetric Bingham fluid flow, let us rewrite the Bingham

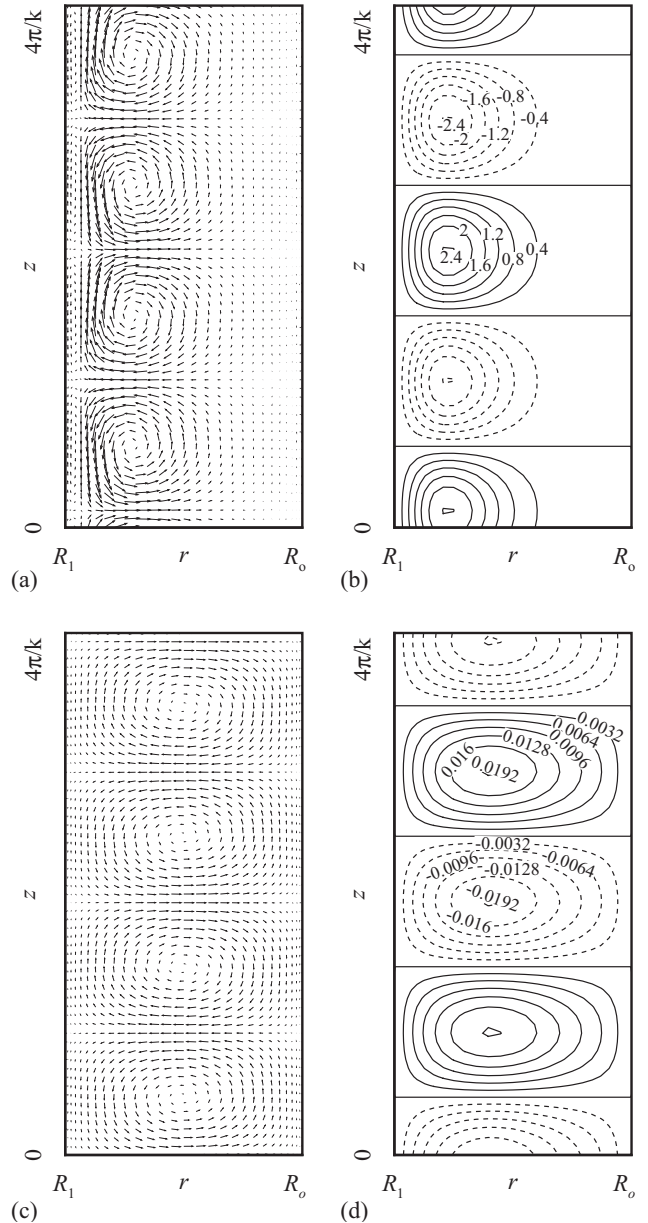


FIG. 5. (a) and (c) Meridional velocity fields and (b) and (d) contours of azimuthal velocity of the optimal inputs at (a) and (b)  $\eta = 0.5$ ,  $Re_1 = 1510$ , and  $k = 10.34$  and (c) and (d)  $\eta = 0.99$ ,  $Re_1 = 340$ , and  $k = 2.82$ .

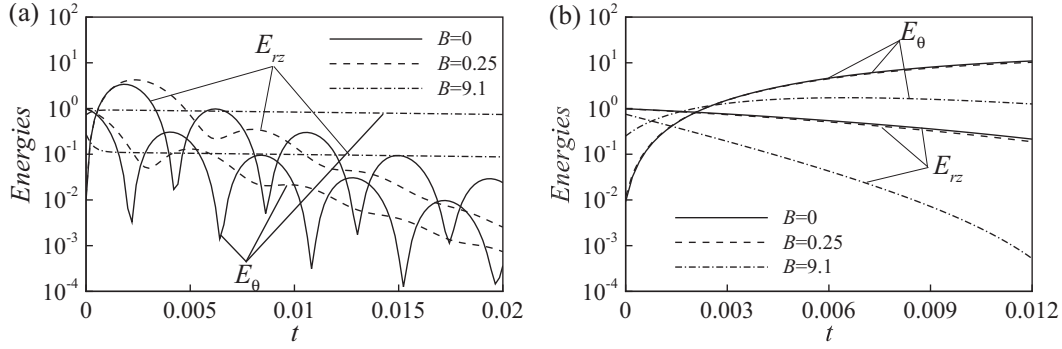


FIG. 6. Time evolution of the energies in the meridional components  $E_{rz}$  and in the azimuthal component  $E_\theta$  of the optimal perturbation for (a)  $\eta = 0.5$ ,  $\text{Re}_1 = 1510$ , and  $k = 10.34$  and (b)  $\eta = 0.99$ ,  $\text{Re}_1 = 340$ , and  $k = 2.82$ .

terms in the equations of the radial and axial directions governing the evolution of perturbations in the meridional plane as

$$\phi_r = \frac{1}{\dot{\gamma}}(DD_* - k^2)u - \frac{D\dot{\gamma}}{\dot{\gamma}^2}\dot{\gamma}_{rr}(\mathbf{u}), \quad (10)$$

$$\phi_z = \frac{1}{\dot{\gamma}}(D_*D - k^2)w - \frac{D\dot{\gamma}}{\dot{\gamma}^2}\dot{\gamma}_{rz}(\mathbf{u}). \quad (11)$$

Note from (10) and (11) that the stress perturbations originating from the nonconstant part of viscosity can be divided into two parts in the meridional plane. The first one corresponds to viscous dissipation with equivalent viscosity  $\frac{B}{\dot{\gamma}(\mathbf{u})}$ , independent of the growth mechanism. The second part represents the additional stress field  $-B\frac{D\dot{\gamma}}{\dot{\gamma}^2}[\dot{\gamma}_{rr}(\mathbf{u}), \dot{\gamma}_{rz}(\mathbf{u})]$  induced by the radial inhomogeneity of the effective viscosity. Taking the divergence of the governing equations (2)-(4) results in the following Poisson equation for the pressure field  $p$ :

$$(D_*D - k^2)p = \text{Re}_1 \frac{1}{r} \frac{\partial}{\partial r}(2r\Omega v) + (D_*D - k^2)\phi, \quad (12)$$

wherein  $\phi$  is the scalar potential of the potential part of the additional stress field. It should now be evident that the pressure force  $[-\partial p/\partial r, -ikp]$  is balanced by the potential part of the sum of local Coriolis force  $2\text{Re}_1\Omega v\mathbf{e}_r$  [27] and additional stress. As a result, the effective force acting on the production of meridional perturbations is its rotational part, which determines the behavior of energy growth.

For the wide-gap case with small  $B$ , Figs. 7(a) and 7(b) show the Coriolis force and its rotational part, which consists of only one array of vortices with larger magnitude of meridional components and the same direction of rotation as the main one in the velocity field of the optimal perturbation for  $B = 0$  [Fig. 5(a)]; Figs. 7(c) and 7(d) plot the additional stress field and its rotational part, in which three arrays of vortices are observed with meridional components significantly weaker. Moreover, both the first and third arrays of vortices (running left to right) rotate in the direction opposite to that in the rotational part of the Coriolis force. In a similar fashion as in Fig. 7, Fig. 8 shows the Coriolis force and its rotational part for large enough  $B$  ( $B = 9.1$ ), together with the additional stress field and its rotational part, which is featured by a single array of vortices [Fig. 8(d)], as is the rotational part of the Coriolis force. Further, the sign of azimuthal vorticity for the rotational part of the additional stress is opposite to that for the rotational

part of the Coriolis force and its meridional components are large such that the production of azimuthal vorticity by the Coriolis force can be nearly canceled. In order to demonstrate the effects of the rotational parts of both the Coriolis force and the additional stress on the energy evolution of meridional perturbation, a quantitative measure of the flow is needed to monitor its change in energy caused by the rotational part of the Coriolis force or the additional stress solely. An appropriate diagnostic quantity is the energy spectrum in the meridional plane ( $|u|^2 + |w|^2$ ) $r$  of the superimposed optimal perturbation  $\mathbf{u}(0) + \mathbf{F}_{\text{rot}} \cdot \Delta t$ , where  $\mathbf{F}_{\text{rot}}$  denotes the rotational part of the Coriolis force or the additional stress and the values of  $\Delta t$ , for the wide-gap case and the narrow-gap case are set to  $10^{-4}$  and  $10^{-2}$ , sufficiently small compared to the time scales during which maximum transient growth is achieved for most sets of the influencing parameters in the scope of this paper. Figure 9 plots the energy spectrum function with  $B = 0.25$  and  $9.1$ , both for the same values of  $k$  and  $\text{Re}_1$  as in Fig. 6(a). We observe that for smaller  $B$ , the rotational part of the Coriolis force is indeed responsible for further production of the azimuthal vorticity and the resulting increase of perturbation energy in the meridional components. In addition, the additional stress and the Coriolis force play counteractive roles in the evolution of meridional perturbations, although it is observed that the presence of additional stress has an insignificant effect on energy evolution and could not eliminate the generation of azimuthal vorticity rolls due to the local Coriolis force because of the weak magnitude of its rotational part and hence the anti-lift-up mechanism still exists. In contrast, for larger  $B$ , the changes in the energy spectrum induced by the additional stress and the Coriolis force are seen to be comparative in magnitude and of opposite sign over most of the radial interval, indicative of a near cancellation of meridional perturbations produced by the rotational part of the Coriolis force. Thus, the perturbation energy in the meridional plane  $E_{rz}$  can no longer increase with time and the lift-up view becomes a reasonable explanation of the transient growth phenomenon [see Fig. 6(a)].

As for the narrow-gap case, Fig. 10 plots the Coriolis force and its rotational part for  $B = 0.25$ , as well as the additional stress field and its rotational part. There is only one array of vortices with larger magnitude of meridional perturbations for the rotational part of the Coriolis force and a pair of counterrotating vortices with much smaller magnitude of meridional perturbations for the rotational part of the additional stress. For  $B = 9.1$  the situation is qualitatively

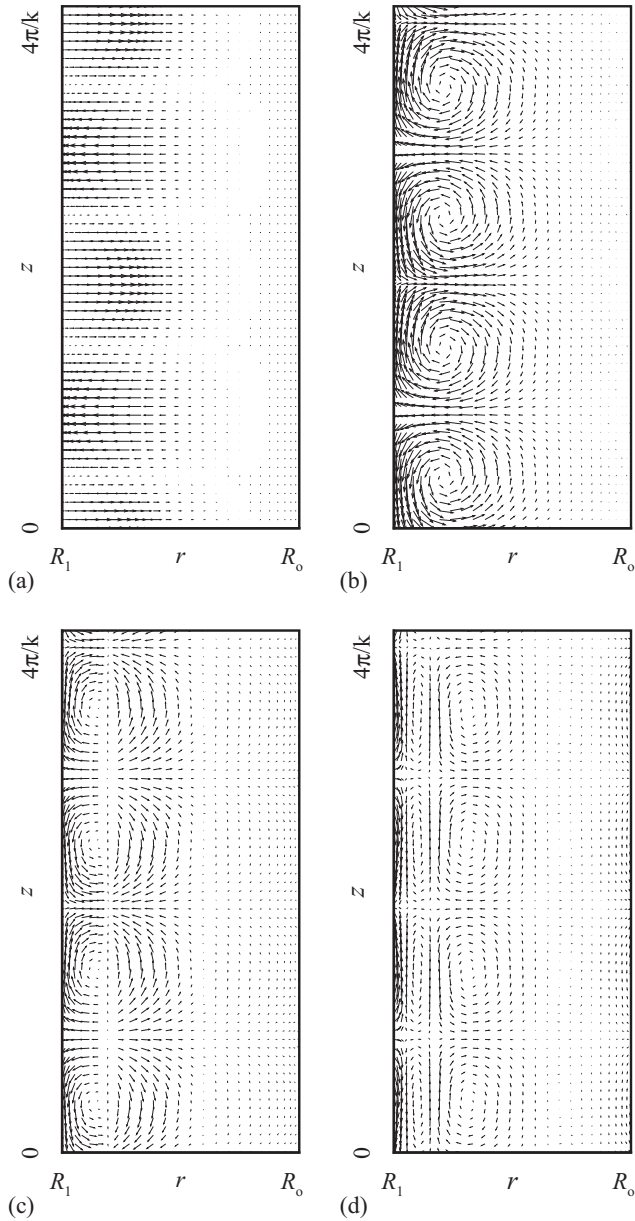


FIG. 7. (a) Radial-axial vector plot of the Coriolis force and its Helmholtz decomposition into (b) the rotational part, (c) the vector plot of the additional stress field, and (d) its rotational part, for  $\eta = 0.5$ ,  $\text{Re}_1 = 1510$ ,  $B = 0.25$ , and  $k = 10.34$ .

similar, except that the magnitude of the rotational part of the additional stress is relatively large, as shown in Fig. 11. To illustrate the energy evolution of meridional perturbations with  $\eta = 0.99$ , Fig. 12 plots the corresponding energy spectra for the cases  $B = 0.25$  and  $9.1$ . It can be seen that the addition of the rotational part of the Coriolis force leads to energy decay in the meridional components of the optimal perturbation, opposite to that observed in the wide-gap case. Further, this damping effect of the Coriolis force is enlarged with the increase of yield stress, while the energy spectrum curves of the superimposed optimal perturbation by the rotational part of the additional stress coincide nearly with those of the original optimal perturbation even in the case of large yield stress,

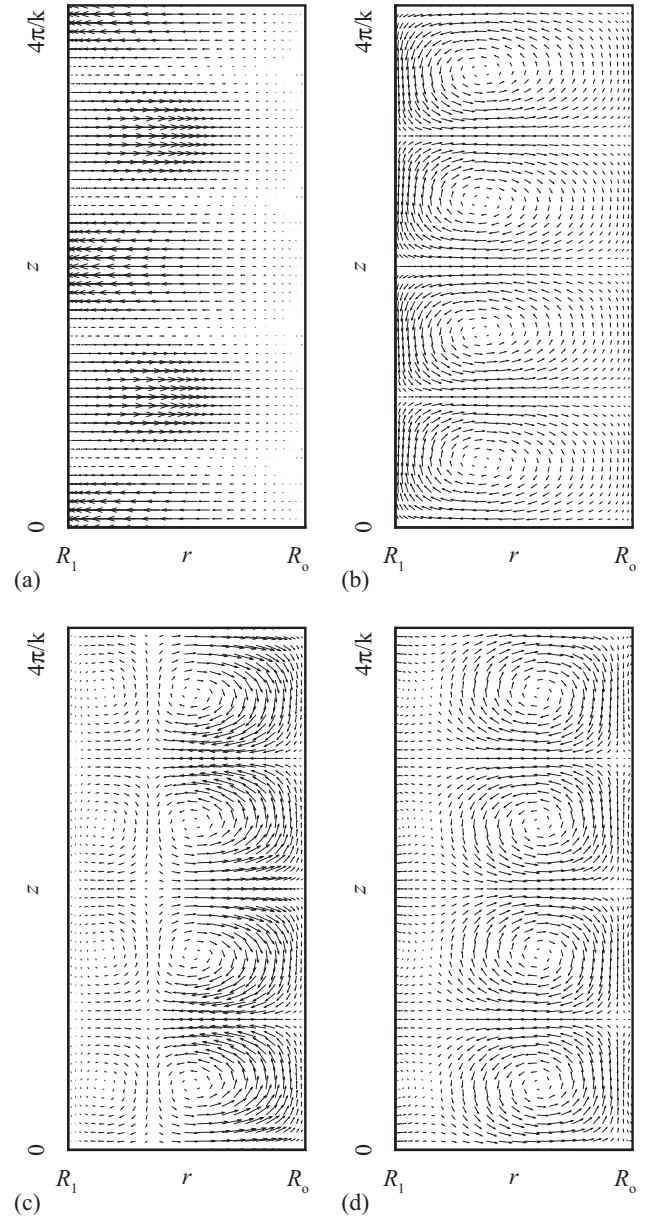


FIG. 8. (a) Radial-axial vector plot of the Coriolis force and its Helmholtz decomposition into (b) the rotational part, (c) the vector plot of the additional stress field, and (d) its rotational part, for  $\eta = 0.5$ ,  $\text{Re}_1 = 1510$ ,  $B = 9.1$ , and  $k = 10.34$ .

implying that it has little influence on the energy spectrum distribution. Thus, the decay rate of perturbation energy in the meridional plane becomes increasingly large with increasing  $B$ , as found earlier in Fig. 6(b).

For the axisymmetric case of counterrotating cylinders, it is also necessary to see how yield stress alters the existing lift-up mechanism [12,14]. Figure 13 plots the variation in the relative amplitude of the azimuthal and radial directions of the optimal perturbation with  $B$  for both wide-gap and narrow-gap counterrotating cylinders. The  $k$  values are chosen at which the maximum  $G_{\text{max}}$  is attained for  $B = 0$ . For the wide-gap case, the larger peak of the perturbed azimuthal velocity is shifted toward the inner cylinder by strong yield

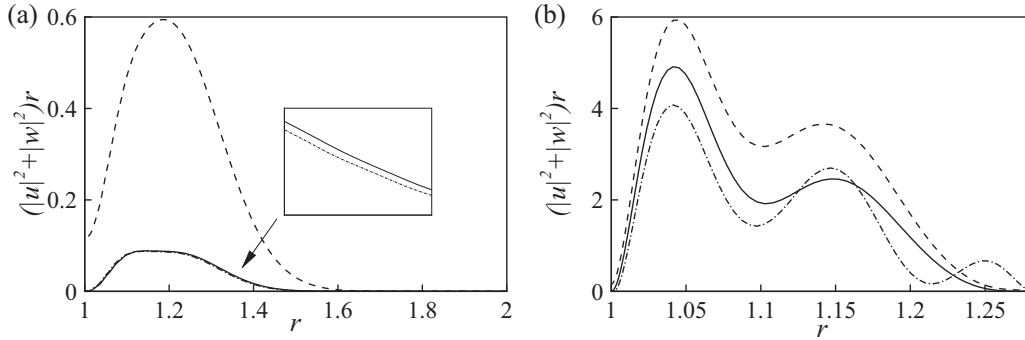


FIG. 9. Radial distribution of the energy spectrum function for the wide-gap case for  $\eta = 0.5$ ,  $\text{Re}_1 = 1510$ ,  $k = 10.34$ , and (a)  $B = 0.25$  and (b)  $B = 9.1$ . In the plots of the energy spectrum function (including Figs. 12 and 15), the solid line is for the original optimal perturbation  $\mathbf{u}(0)$ , the dashed line is for the superimposed optimal perturbation by the rotational part of the Coriolis force, and the dash-dotted line is for the superimposed optimal perturbation by the rotational part of the additional stress field.

stress ultimately and the lower one is damped gradually. In contrast, for the narrow-gap case, the lower peak value of the azimuthal component decreases with increasing  $B$  as the larger peak shifts to higher  $r$ . In addition, the shifting of the peak values is likewise observable for the amplitude of the perturbed radial velocity, as shown in Figs. 13(b) and 13(d). It should be noted that the trends of inward (the wide-gap case) and outward (the narrow-gap case) shifts of the amplitude of optimal perturbation are consistent with those observed in the corotating scenario discussed before.

Figure 14 plots the energy evolutions  $E_{rz}$  and  $E_\theta$  with  $B = 0, 1$ , and  $9$  for both the wide-gap case and the narrow-gap case. It appears obvious that the yield stress may not change the physical mechanism underlying such energy growth (i.e., the lift-up effect) in both cases, similar to that seen in the narrow-gap case of corotating Taylor-Couette flow [Fig. 6(b)]. Further, it is also clear that both  $E_{rz}$  and  $E_\theta$  are greatly suppressed by the yield stress dissipation [17]. Figure 15 plots the energy spectrum functions only for  $B = 9$ , as the rotational parts of both the Coriolis force and the additional stress seem to have almost no effect on energy evolution for relatively weak yield stress. There is some similarity between the types of influence of the rotational parts on the energy spectrum distribution in the case of counterrotating cylinders and in the narrow-gap case of corotating cylinders, where the lift-up mechanism has been found previously. That is, for both the wide-gap case and the narrow-gap case, the rotational part of the Coriolis force causes the decrease of perturbation energy in the meridional plane despite its lower magnitude compared to that derived in the narrow-gap case of corotating cylinders and the change of perturbation energy induced by the rotational part of the additional stress is invisible even for large  $B$ .

Having examined optimal mode growth mechanisms in the axisymmetric case, we now turn to the oblique modes with emphasis on the case of counterrotation, where non-normal transient growth is more significant due to stronger shear effects compared to that for corotating cylinders. The values of parameters, including  $\text{Re}_1$ ,  $\text{Re}_2$ ,  $B$ , and  $k$ , are the same as for  $m = 0$ . The  $G(t)$  curves are given for both the wide-gap case and the narrow-gap case in Fig. 16, which provides the optimal growth with different azimuthal wave numbers ranging from  $m = 0$  to  $10$ . Note that the axisymmetric mode

does not exhibit a substantial growth, in comparison with other spiral nonaxisymmetric modes. For the wide-gap case with  $B = 0$ , the extreme  $G_{\text{opt}}$  of  $G(t)$  increases with increasing  $m$  until  $m = 3$  is reached, where  $G_{\text{opt}}$  is maximized, while  $G_{\text{opt}}$  decreases with increasing  $m$  obviously for larger  $m$ . This observation is similar to the results found by Meseguer [14], which demonstrates that nonaxisymmetric nonmodal perturbations can be dominant for the Newtonian fluid with  $\eta = 0.881$ . Further, the optimal azimuthal mode, which is featured by the maximum  $G_{\text{opt}}$ , may change with increasing yield stress. As can be seen in Fig. 16(b), the optimal azimuthal mode becomes the eigenmode  $m = 4$  with  $B = 1$ . Figure 17 plots the axial vorticity perturbation  $\omega_z$  of the optimal input  $\mathbf{u}(0)$  and its output  $\mathbf{u}(t_{\text{opt}})$  at the corresponding optimal time for  $B = 0$  and  $1$ . This perturbation is at  $t = 0$  composed of a set of spiraling vorticity sheets close to the inner cylinder wall that evolve so as to produce a strong helical wave in both cases. As time flows, the initial spirals are advected and unfolded via the three-dimensional mechanism of vortex tilting and stretching [28], which accounts for a local reorganization of the perturbation vorticity and the growth of transient  $m = 3$  or  $4$  perturbations. The situations of narrow gap ( $\eta = 0.99$ ) are also analyzed for the purpose of comparison. The results imply that  $G_{\text{opt}}$  increases monotonically with the increase of  $m$  despite the magnitude of yield stress, as shown in Figs. 16(c) and 16(d), although the flow may become linearly unstable with increasing  $m$  at small  $B$ .

To understand how yield stress can affect the results of growth characteristics of oblique modes, Fig. 18 plots the variation of the amplitude of optimal perturbation with  $B$  for the eigenmode  $m = 3$ , which is representative at the selected set of values of the parameters for the wide-gap case. The peak of the amplitude of optimal perturbation is shifted toward the inner cylinder with increasing yield stress for the wide-gap case ( $\eta = 0.5$ ) and the trend is opposite for the narrow-gap case ( $\eta = 0.99$ ), consistent with the axisymmetric scenario.

Next, let us consider the effect of yield stress on the transient growth mechanism for oblique modes. Before proceeding to the related results, it is necessary to derive the linear energy equality first. On multiplying (2)–(4) by  $r$  times the complex conjugate  $\bar{\mathbf{u}} = (\bar{u}, \bar{v}, \bar{w})$  and then integrating from  $R_1$  to  $R_o$ , we

derive

$$dE/dt = \text{Re}_1 J_I - J_V - B J_Y, \quad (13)$$

where  $E$  is the energy norm defined by (8) and  $J_I$ ,  $J_V$ , and  $J_Y$  denote inertial, viscous, and yield stress contributions to the kinetic energy growth of the perturbations. These are defined by

$$J_I = -\frac{1}{4} \int_{R_1}^{R_o} \left( DV - \frac{V}{r} \right) (\bar{u}v + \bar{v}u) r dr, \quad (14)$$

$$J_V = \frac{1}{2} \int_{R_1}^{R_o} \left( |D\mathbf{u}|^2 + k^2 |\mathbf{u}|^2 + \frac{m^2 |\mathbf{u}|^2}{r^2} + \frac{|u|^2 + |v|^2}{r^2} + \frac{2im(\bar{u}v - \bar{v}u)}{r^2} \right) r dr, \quad (15)$$

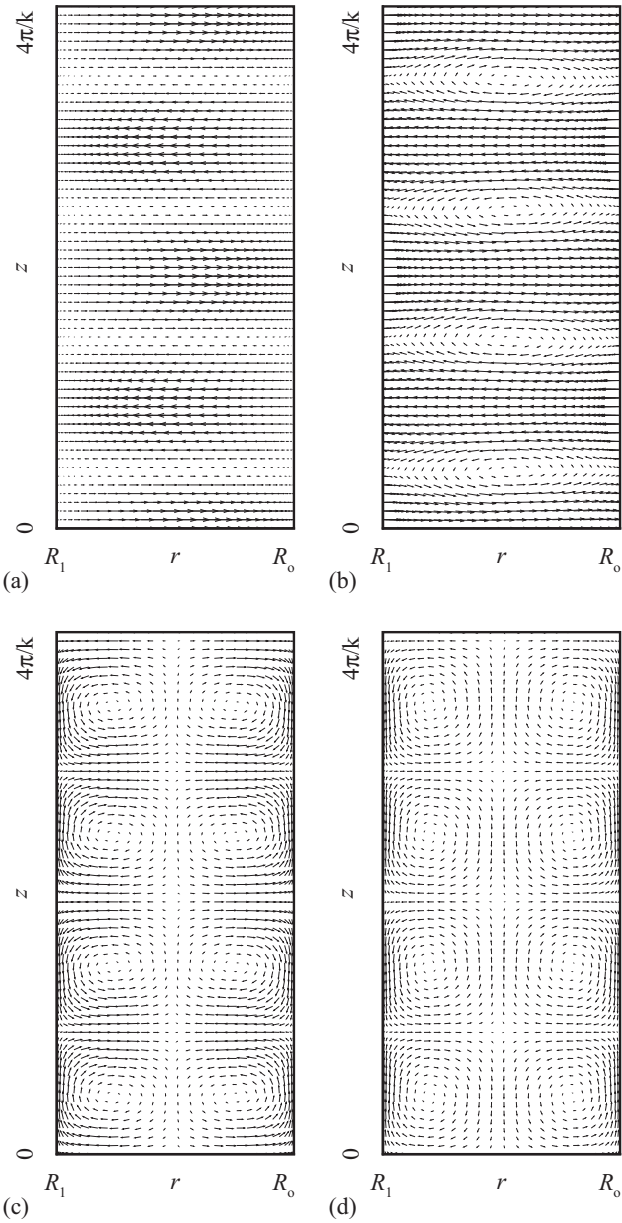


FIG. 10. (a) Radial-axial vector plot of the Coriolis force and its Helmholtz decomposition into (b) the rotational part, (c) the vector plot of the additional stress field, and (d) its rotational part, for  $\eta = 0.99$ ,  $\text{Re}_1 = 340$ ,  $B = 0.25$ , and  $k = 2.82$ .

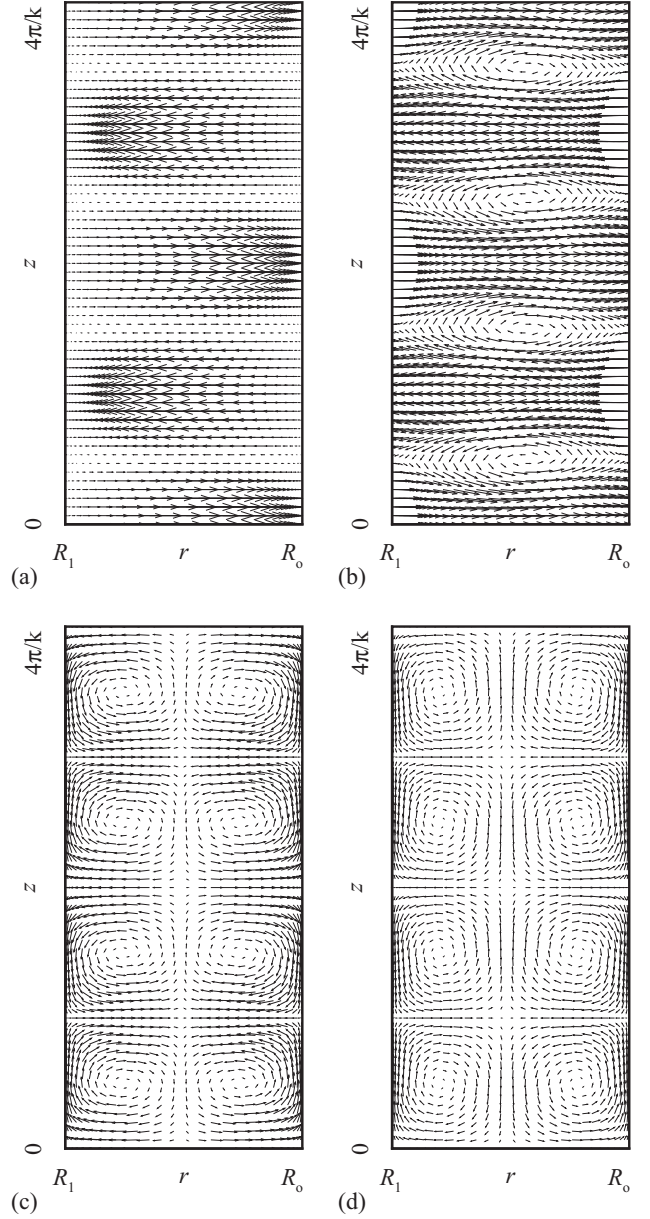


FIG. 11. (a) Radial-axial vector plot of the Coriolis force and its Helmholtz decomposition into (b) the rotational part, (c) the vector plot of the additional stress field, and (d) its rotational part, for  $\eta = 0.99$ ,  $\text{Re}_1 = 340$ ,  $B = 9.1$ , and  $k = 2.82$ .

$$J_Y = \frac{1}{2} \int_{R_1}^{R_o} \frac{1}{\dot{\gamma}} \left[ 2 \left( |Du|^2 + \frac{|u|^2}{r^2} \right) + k^2 (|v|^2 + 2|w|^2) + |ku - iDw|^2 + \frac{2im(\bar{u}v - \bar{v}u)}{r^2} + \frac{m^2 (2|v|^2 + |w|^2)}{r^2} + \frac{mk(\bar{v}w + \bar{w}v)}{r} \right] r dr. \quad (16)$$

Note that the sign of  $\dot{\gamma}_{r\theta} = DV - \frac{V}{r}$  is the same as that of both  $\tau_{r\theta}$  and  $\frac{\Omega_2}{\Omega_1} - 1$  and in the case of counterrotation it must be negative. That is,  $\dot{\gamma} = |\dot{\gamma}_{r\theta}| = - (DV - \frac{V}{r})$ . Substituting

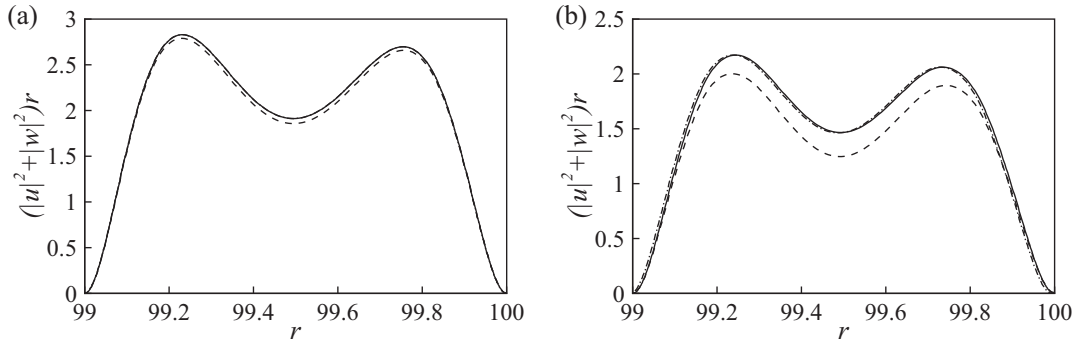


FIG. 12. Radial distribution of the energy spectrum function for the narrow-gap case for  $\eta = 0.99$ ,  $Re_1 = 340$ ,  $k = 2.82$ , and (a)  $B = 0.25$  and (b)  $B = 9.1$ .

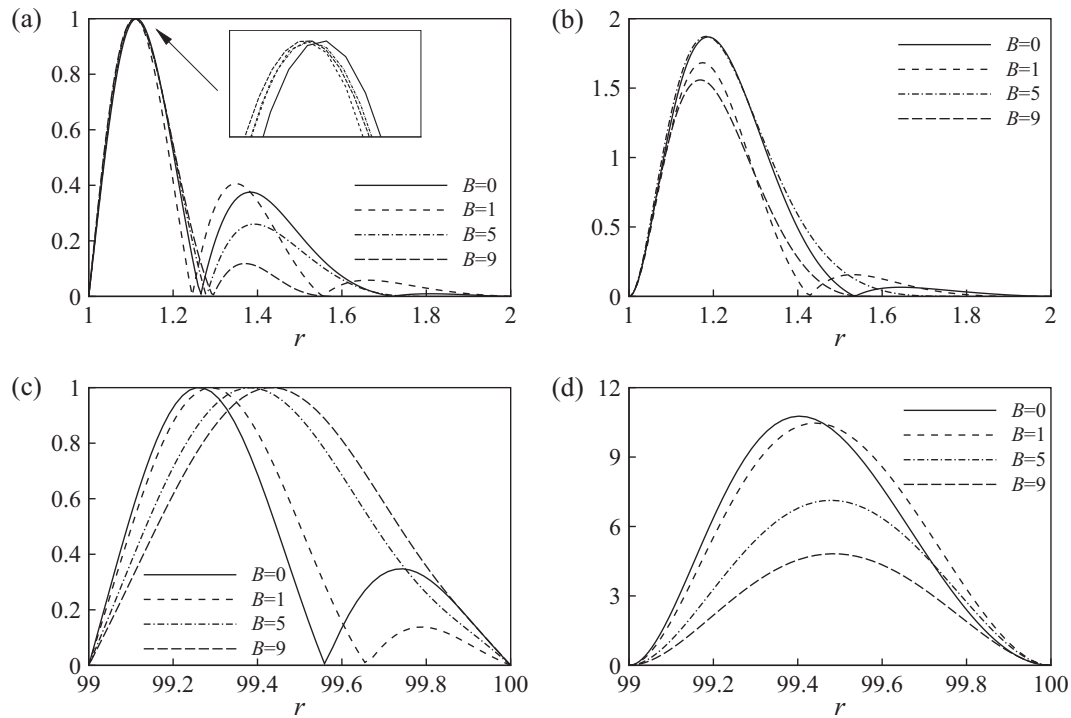


FIG. 13. Amplitudes of the (a) and (c) azimuthal and (b) and (d) radial directions of the optimal perturbation for counterrotating cylinders at (a) and (b)  $\eta = 0.5$ ,  $Re_1 = 320$ , and  $k = 8.34$  and (c) and (d)  $\eta = 0.99$ ,  $Re_1 = 800$ , and  $k = 3.68$ .

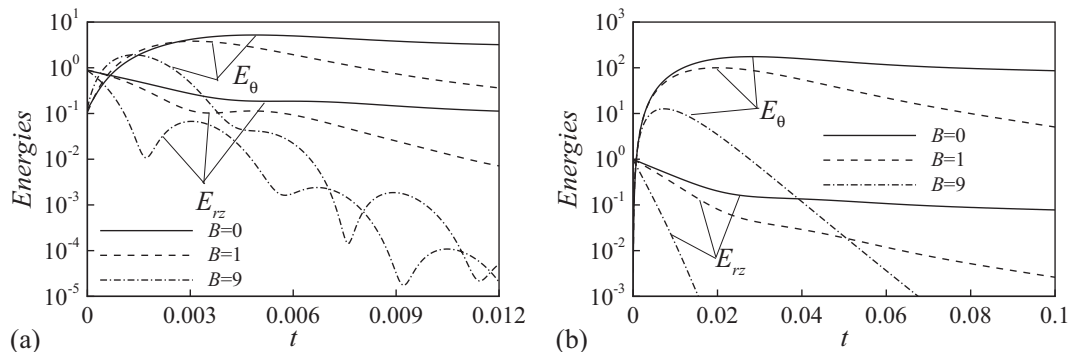


FIG. 14. Time evolution of the energies in the meridional components  $E_{rz}$  and in the azimuthal component  $E_\theta$  of the optimal perturbation for counterrotating cylinders for (a)  $\eta = 0.5$ ,  $Re_1 = 320$ , and  $k = 8.34$  and (b)  $\eta = 0.99$ ,  $Re_1 = 800$ , and  $k = 3.68$ .

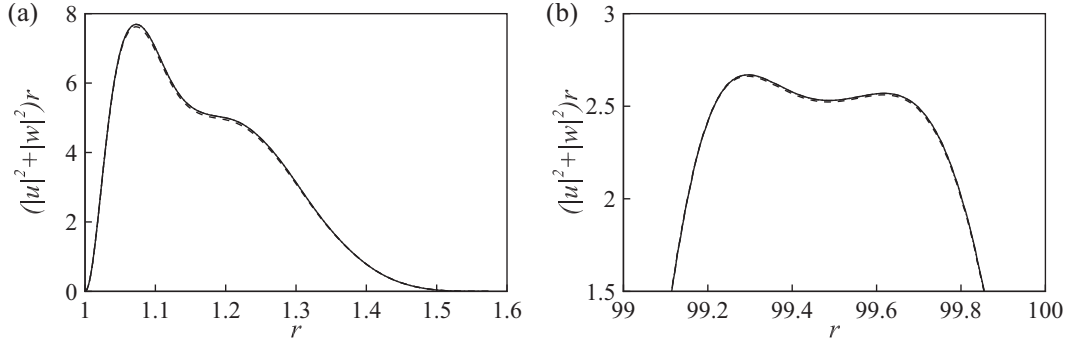


FIG. 15. Radial distribution of the energy spectrum function for counterrotating cylinders for  $B = 9$  and (a)  $\eta = 0.5$ ,  $\text{Re}_1 = 320$ , and  $k = 8.34$  and (b)  $\eta = 0.99$ ,  $\text{Re}_1 = 800$ , and  $k = 3.68$ .

this expression into (14), we have

$$J_I = \frac{1}{4} \int_{R_1}^{R_o} \dot{\gamma}(\bar{u}v + \bar{v}u)r dr = \frac{1}{2} \int_{R_1}^{R_o} \dot{\gamma}(u_R v_R + u_I v_I)r dr, \quad (17)$$

where the subscripts  $R$  and  $I$  represent the real and imaginary parts of the complex amplitude, respectively. The time evolutions of  $\text{Re}_1 J_I$ ,  $J_V$ , and  $B J_Y$  are depicted in Fig. 19 to study the effects of them on the evolutionary energy growth for oblique modes with  $\eta = 0.5$  and four  $B$  values ( $B = 0, 1, 5, \text{ and } 9$ ). With increasing  $B$ , there is a decrease in the magnitudes of  $\text{Re}_1 J_I$  and  $J_V$  as well as an increase in that of  $B J_Y$  [Figs. 19(a)–19(c)]. This trend seems to hold for modes  $m = 3$  and 4. Further, in the absence of yield stress, the energy growth is only determined by the viscous dissipative term  $J_V$  and the inertial term  $\text{Re}_1 J_I$ . Although the growth rate  $dE/dt$  for  $m = 4$  mode is larger than that for the  $m = 3$  case during an initial time period, as expected due to larger  $\text{Re}_1 J_I$ , the arrest

of growth occurs faster for the former because of the quicker decay of  $\text{Re}_1 J_I$  [Fig. 19(d)]. Consequently, the optimal perturbation for the mode  $m = 3$  is found to achieve a slightly larger amplification level than that for the mode  $m = 4$ , as can be seen in Fig. 16(a). At larger  $B$  ( $B = 1$ ), the decay rate of  $\text{Re}_1 J_I$  and the time of growth arrest for the mode  $m = 4$  are nearly the same as for  $m = 3$  and initially the former has larger positive  $\text{Re}_1 J_I$  magnitude. Hence, the mode  $m = 4$  is featured by a larger optimal energy growth  $G_{\text{opt}}$  than the mode  $m = 3$ , as shown in Fig. 16(b), despite the fact that the increase of  $B J_Y$  for the former is more significant and induces greater cancellation of energy growth rate generated by the inertial term. With stronger yield stress ( $B = 5, 9$ ), which makes an unyielded plug arise on the outer wall, the behavior of energy growth (such as  $\text{Re}_1 J_I$  and  $dE/dt$  curves) for the mode  $m = 3$  is quite close to that for the mode  $m = 4$ . The variations of  $\text{Re}_1 J_I$ ,  $J_V$ ,  $B J_Y$ , and  $dE/dt$  with time for the narrow-gap case are also plotted in Fig. 20, focusing on the axisymmetric mode  $m = 0$

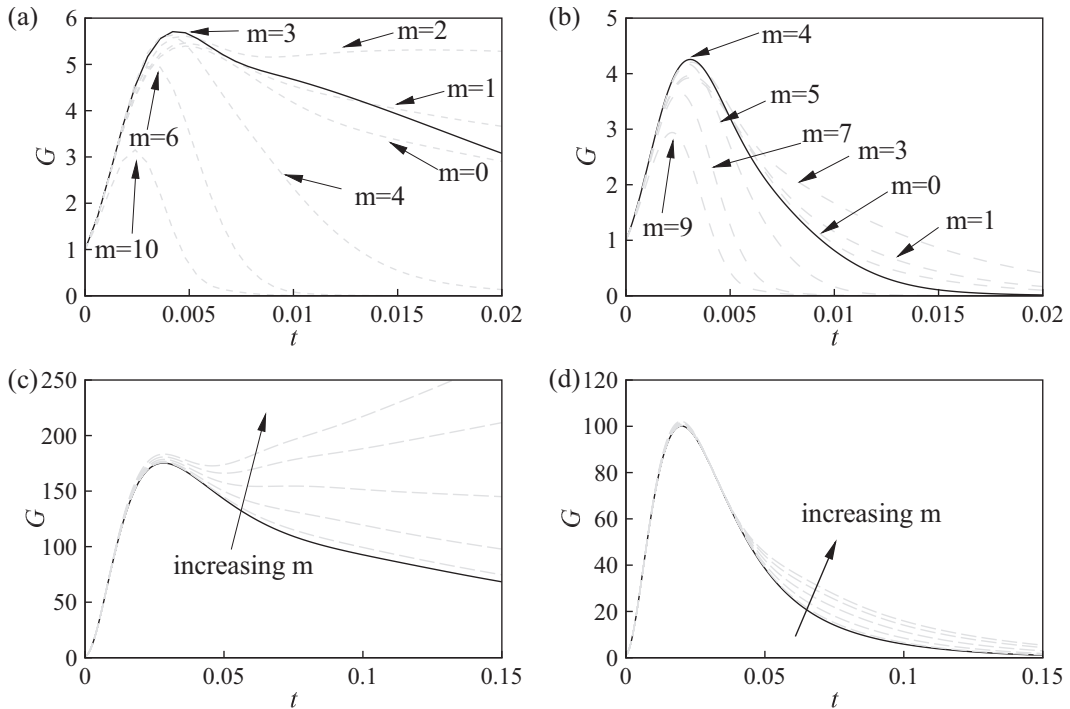


FIG. 16. The  $G(t)$  curves with different azimuthal wave numbers for the (a) and (c)  $B = 0$  and (b) and (d)  $B = 1$  cases at (a) and (b)  $\eta = 0.5$ ,  $\text{Re}_1 = 320$ , and  $k = 8.34$  and (c) and (d)  $\eta = 0.99$ ,  $\text{Re}_1 = 800$ ,  $k = 3.68$ .

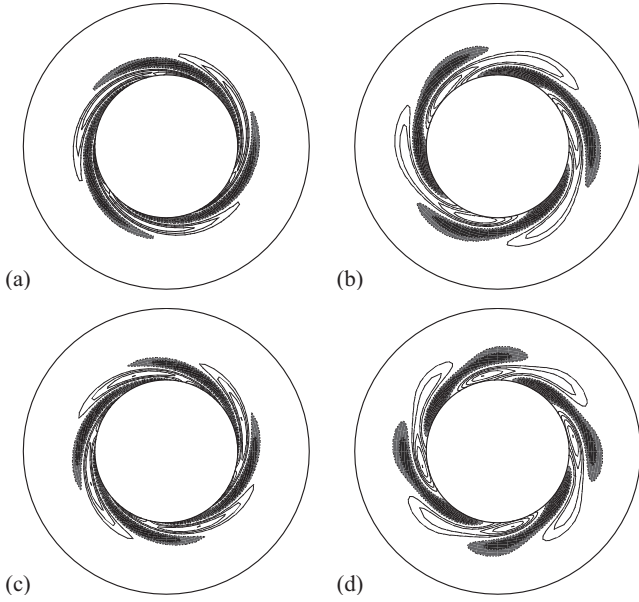


FIG. 17. Axial vorticity  $\omega_z$  contours of (a) and (c) the optimal perturbation  $\mathbf{u}(0)$  and (b) and (d) its output  $\mathbf{u}(t_{\text{opt}})$  at the corresponding optimal time at  $\eta = 0.5$ ,  $\text{Re}_1 = 320$ , and  $k = 8.34$  and (a) and (b)  $B = 0$  and (c) and (d)  $B = 1$ . Shaded regions and dashed lines denote negative vorticity. Contour levels are (a)  $[\pm 5.62, \pm 28.1, 5.62]$ , (b)  $[\pm 4.64, \pm 23.2, 4.64]$ , (c)  $[\pm 6.26, \pm 31.3, 6.26]$ , and (d)  $[\pm 4.28, \pm 21.4, 4.28]$ .

and the mode  $m = 1$ . A comparison of the results of the two eigenmodes shows that the trends of energy growth for both are quantitatively similar, as can be seen in Figs. 20(a)–20(c). Further, the arrest of growth for the mode  $m = 1$  always occurs at later times compared to the axisymmetric mode [Fig. 20(d)],

no matter how strong the yield stress is considered, although the former mode has a slightly smaller  $\text{Re}_1 J_I$  magnitude in the initial period. As a result, the integrated positive energy growth for the mode  $m = 1$  is increased compared to the axisymmetric mode, as shown in Figs. 16(c) and 16(d).

#### IV. SUMMARY AND CONCLUSIONS

In summary, we have studied the transient growth characteristics of the Taylor-Couette flow of a Bingham fluid for two values of  $\eta$ , i.e., the wide-gap case with  $\eta = 0.5$  and the narrow-gap case with  $\eta = 0.99$ . By solving the initial value problem, we have shown that the effects of yield stress on the energy transient growth and flow structure of the optimal perturbations are quite different for the two cases. Considering axisymmetric optimal modes for corotating cylinders, the peak of the amplitude of optimal perturbation is found to be shifted toward the inner cylinder with increasing yield stress  $B$  for the wide-gap case. Further, the anti-lift-up mechanism along with large  $\text{Re}_1$  cannot be observed when strong yield stress is imposed, as the production of meridional perturbations due to local Coriolis force is largely suppressed by the increase of the additional stress field formed from an inhomogeneous distribution of the effective viscosity. The situation for the narrow-gap case is quite different: The peak value of the amplitude of the optimal perturbation is shifted toward the outer cylinder with increasing  $B$ . Moreover, the rotational part of the Coriolis force induces energy decay in the meridional components of the optimal perturbation, opposite to that observed in the wide-gap case. This damping effect of the Coriolis force is enlarged with the increase of  $B$  and the rotational part of the additional stress has little influence on the energy growth behavior, leading to

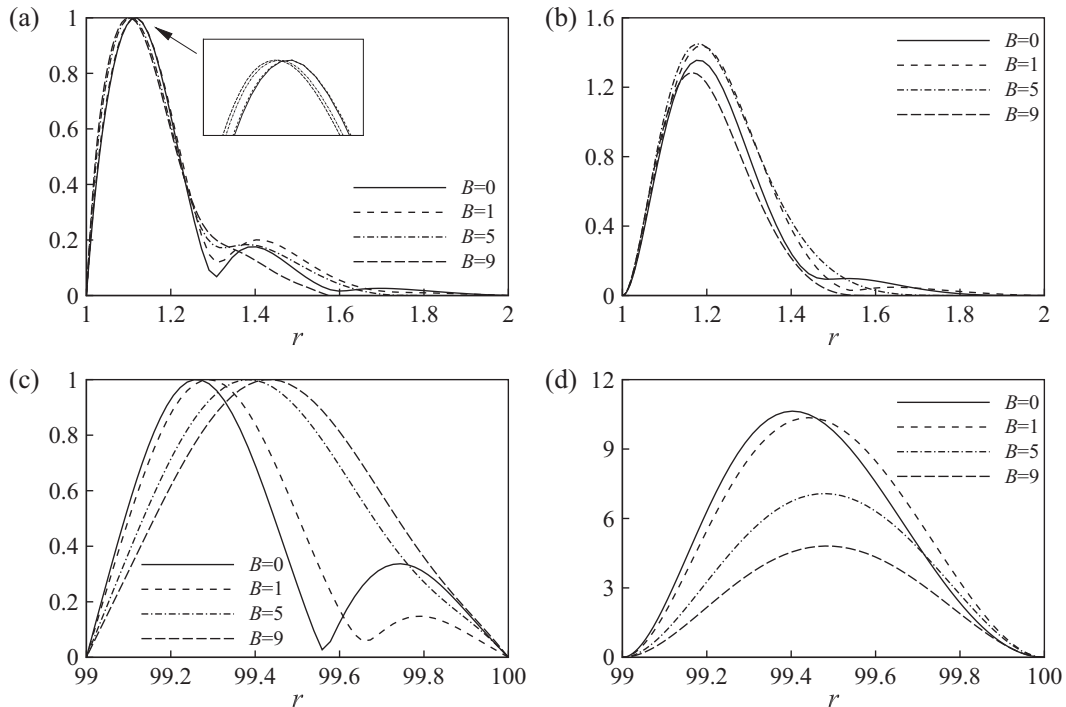


FIG. 18. Amplitudes of the (a) and (c) azimuthal and (b) and (d) radial directions of the optimal perturbation for the eigenmode  $m = 3$  at (a) and (b)  $\eta = 0.5$ ,  $\text{Re}_1 = 320$ , and  $k = 8.34$  and (c) and (d)  $\eta = 0.99$ ,  $\text{Re}_1 = 800$ , and  $k = 3.68$ .

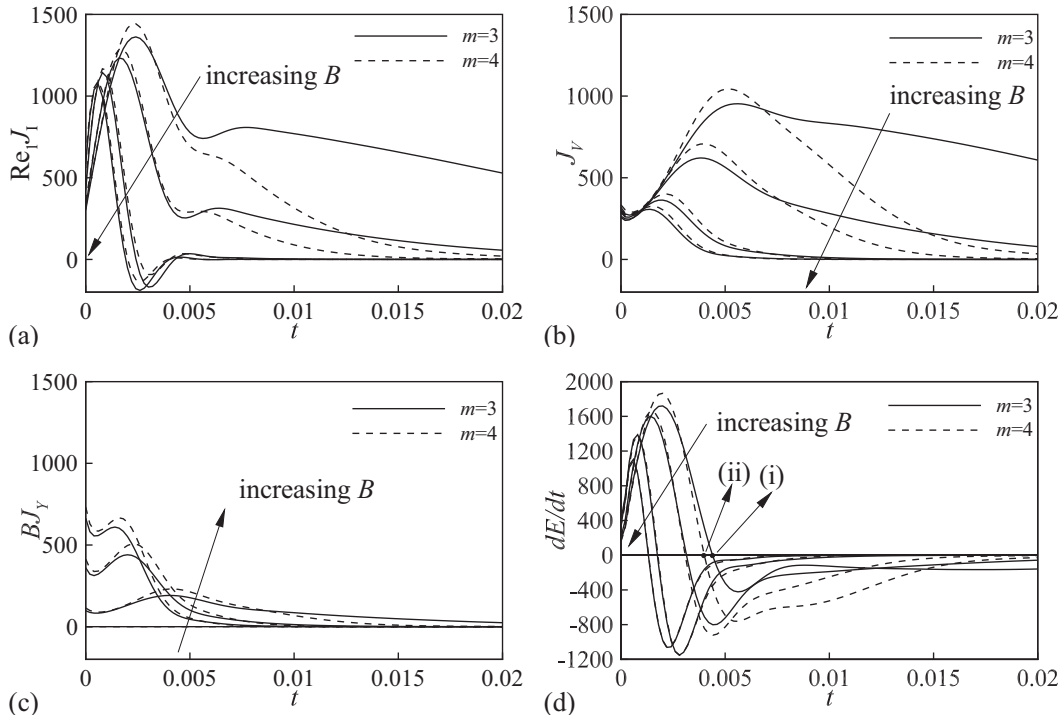


FIG. 19. Time evolution of the inertial term  $Re_1 J_I$ , the viscous dissipative term  $J_V$ , the yield stress dissipative term  $B J_Y$ , and the energy growth rate  $dE/dt$  for the modes  $m = 3$  and 4 with  $\eta = 0.5$ ,  $Re_1 = 320$ , and  $k = 8.34$ , and  $B = 0, 1, 5$ , and 9. The time of the arrest of energy growth for the modes (i)  $m = 3$  and (ii)  $m = 4$  with  $B = 0$  are indicated.

the increase of the decay rate of perturbation energy in the meridional plane with increasing  $B$ .

We have also carried out the transient growth analysis for the axisymmetric case with counterrotating cylinders.

As expected, the trends of inward (the wide-gap case) and outward (the narrow-gap case) shifts of the amplitude of optimal perturbation are consistent with those observed in the corotating scenario. Further, the influence of the rotational

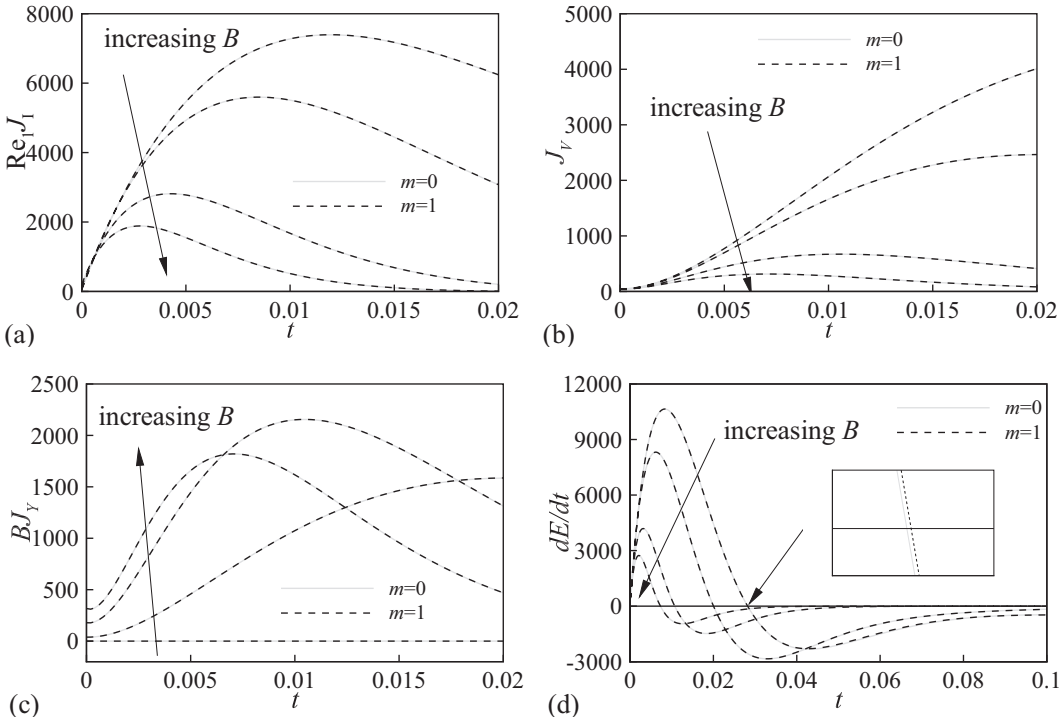


FIG. 20. Time evolution of the inertial term  $Re_1 J_I$ , the viscous dissipative term  $J_V$ , the yield stress dissipative term  $B J_Y$ , and the energy growth rate  $dE/dt$  for the modes  $m = 0$  and 1 with  $\eta = 0.99$ ,  $Re_1 = 800$ ,  $k = 3.68$ , and  $B = 0, 1, 5$  and 9.

parts on the energy evolution in the case of counterrotating cylinders is very similar to that in the narrow-gap case of corotating cylinders, as can be seen from the corresponding plot of energy spectrum (Fig. 15).

Compared to the axisymmetric mode, spiral nonaxisymmetric modes exhibit more substantial transient growth. Further, the optimal azimuthal mode, which is featured by the maximum  $G_{\text{opt}}$ , changes with increasing yield stress for the wide-gap case. In contrast, for the narrow-gap case,  $G_{\text{opt}}$  increases monotonically with the increase of azimuthal wave number  $m$  despite the magnitude of the yield stress. Also, the inertial, viscous, and yield stress contributions to the kinetic

energy growth are plotted to depict their variations with  $B$  and  $m$ , providing the explanations for the possible change of the optimal azimuthal mode with yield stress.

#### ACKNOWLEDGMENTS

The authors wish to thank Arnaud Antkowiak for his help in improving this paper. Support from the National Natural Science Foundation of China under Grants No. 11402284, No. 11232011, and No. 11402262 and from the China Postdoctoral Science Foundation under Grant No. 2014M561833 is gratefully acknowledged.

- 
- [1] K. Coughlin and P. S. Marcus, *Phys. Rev. Lett.* **77**, 2214 (1996).
  - [2] H. Faisst and B. Eckhardt, *Phys. Rev. E* **61**, 7227 (2000).
  - [3] A. Goharzadeh and I. Mutabazi, *Eur. Phys. J. B* **19**, 157 (2001).
  - [4] A. Prigent, G. Gregoire, H. Chate, O. Dauchot, and W. van Saarloos, *Phys. Rev. Lett.* **89**, 014501 (2002).
  - [5] A. Meseguer, F. Mellibovsky, M. Avila, and F. Marques, *Phys. Rev. E* **79**, 036309 (2009).
  - [6] A. Meseguer, F. Mellibovsky, M. Avila, and F. Marques, *Phys. Rev. E* **80**, 046315 (2009).
  - [7] D. Coles, *J. Fluid Mech.* **21**, 385 (1965).
  - [8] C. Van Atta, *J. Fluid Mech.* **25**, 495 (1966).
  - [9] C. D. Andereck, S. S. Liu, and H. L. Swinney, *J. Fluid Mech.* **164**, 155 (1986).
  - [10] J. J. Hegseth, C. D. Andereck, F. Hayot, and Y. Pomeau, *Phys. Rev. Lett.* **62**, 257 (1989).
  - [11] T. Kato, *Perturbation Theory for Linear Operators* (Springer, New York, 1976).
  - [12] H. Hristova, S. Roch, P. J. Schmid, and L. S. Tuckerman, *Phys. Fluids* **14**, 3475 (2002).
  - [13] H. Hristova, S. Roch, P. J. Schmid, and L. S. Tuckerman, *Theor. Comput. Fluid Dyn.* **16**, 43 (2002).
  - [14] A. Meseguer, *Phys. Fluids* **14**, 1655 (2002).
  - [15] A. Meseguer, *Theor. Comput. Fluid Dyn.* **16**, 71 (2002).
  - [16] M. P. Landry, M.Sc. thesis, University of British Columbia, 2003.
  - [17] M. P. Landry, I. A. Frigaard, and D. M. Martinez, *J. Fluid Mech.* **560**, 321 (2006).
  - [18] J. Peng and K. Q. Zhu, *J. Fluid Mech.* **512**, 21 (2004).
  - [19] W. P. Graebel, in *Proceedings of International Symposium on Second Order Effects in Elasticity, Plasticity and Fluid Dynamics*, edited by M. Reiner and D. Abir (Jerusalem Academic Press, Jerusalem, 1964).
  - [20] C. Nouar, N. Kabouya, J. Dusek, and M. Mamou, *J. Fluid Mech.* **577**, 211 (2007).
  - [21] P. Chossat and G. Iooss, *The Couette-Taylor Problem* (Springer, New York, 1994).
  - [22] R. B. Bird, G. C. Dai, and B. J. Yarusso, *Rev. Chem. Eng.* **1**, 1 (1983).
  - [23] C. Chen, Z. W. Guo, B. F. Wang, and D. J. Sun, *Chin. Phys. Lett.* **28**, 054703 (2011).
  - [24] C. Canuto, M. Y. Hussaini, A. Quarteroni, and T. A. Zang, *Spectral Methods in Fluid Dynamics* (Springer, New York, 1988).
  - [25] P. J. Schmid and D. S. Henningson, *Stability and Transition in Shear Flows* (Springer, New York, 2001).
  - [26] A. Antkowiak, Ph.D. thesis, Université Paul Sabatier, 2005.
  - [27] A. Antkowiak and P. Brancher, *J. Fluid Mech.* **578**, 295 (2007).
  - [28] D. S. Pradeep and F. Hussain, *J. Fluid Mech.* **550**, 251 (2006).